

3D-Printing of non-cytotoxic high-resolution microchannels in bisphenol-A ethoxylate dimethacrylate tissue-mimicking materials

Roger Domingo-Roca^{*a}, Lauren Gilmour^a, Oana Dobre^b, Stylianos Sarrigiannidis^b, Mairi E. Sandison^a, Richard O'Leary^c Joseph C. Jackson-Camargo^c, Helen E. Mulvana^a

^a Department of Biomedical Engineering, University of Strathclyde, Glasgow.

^b James Watt School of Engineering, University of Glasgow, Glasgow.

^c Department of Electronic and Electrical Engineering, University of Strathclyde, Glasgow.

* Corresponding author: Roger Domingo-Roca, 106, Rottenrow Street, G4 0NW, Glasgow, roger.domingo-roca@strath.ac.uk

Email list: roger.domingo-roca@strath.ac.uk, lauren.gilmour@strath.ac.uk, oana.dobre@glasgow.ac.uk, 2022917S@student.gla.ac.uk, mairi.sandison@strath.ac.uk, richard.o-leary@strath.ac.uk, joseph.jackson@strath.ac.uk, helen.mulvana@strath.ac.uk

Keywords: 3D-printing ; hydrogel ; BEMA ; microfluidics; microvasculature

Short running title: 3D-Printing of non-cytotoxic microchannels

Abstract

The ability to create cell-laden fluidic models that mimic the geometries and physical properties of vascularised tissue would be extremely beneficial to the study of disease aetiologies and future therapies, including in the case of cancer where there is increasing interest in studying alterations to the microvasculature. Engineered systems can present significant advantages over animal studies, alleviating challenges associated with variable complexity and control. 3D-printable tissue-mimicking hydrogels can offer an alternative, where control of the biophysical properties of the materials can be achieved. Hydrogel-based systems that can re-create complex, three-dimensional structures and channels with diameters below 500 μm are challenging to produce. We present a non-cytotoxic, photo-responsive hydrogel that supports 3D-printing of complex three-dimensional structures with microchannels down to 150 μm in diameter. Fine tuning of the 3D-printing process has allowed the production of complex structures, where for demonstration purposes we present a helical channel with diameters between 250 and 370 microns around a central channel of 150 microns in diameter in materials with mechanical and acoustic properties that closely replicate those of tissue. The ability to control and accurately reproduce the complex features of the microvasculature has value across a wide range of biomedical applications, especially when the materials involved accurately mimic the physical properties of tissue. An approach that is additionally cell-compatible provides a unique set up that can be exploited to study aspects of biomedical research with an unprecedented level of accuracy.

Introduction

Investigations into the biophysics of fluid flow, gas exchange, and other circulatory phenomena within the microvasculature of animals is hugely important for many areas of biomedical research, not least to develop our understanding of diseases and their treatment. However, fluid-dynamic investigation of biologically relevant channels at the smallest scale is challenging and, in many cases, adequate experimental systems are not available such that simulation studies predominate¹⁻³. Animal testing often remains the only realistic option to investigate networks of the smallest vessels (with diameters of the order of 10 μm) but forces researchers to work with complex fluidic systems that are challenging to control and access. *In vitro* alternatives would be beneficial to improve the specificity of the experiment, the pace at which experiments can be carried out, and ensure ethical considerations can be best met. Advances in computational multiphysics-based simulation software has led to *in silico* techniques becoming a central resource for investigating biological fluid-flows, but validation remains a challenge⁴. There remains no practical way to test outcomes from theoretical and/or simulation studies within complex vessel networks without animal testing, and certainly no way to do this in an agile manner. Thus, a clear need exists for controlled, physiologically-relevant *in vitro* platforms, which can be produced quickly and at low cost, to facilitate iterative microvasculature experimental research.

This is not a trivial task, due in part to the highly complex 3D geometry of the circulatory system. Blood convective transport, which is fundamental for drug transport, is highly affected by microvascular tortuosity^{5,6}, adding an extra degree of complexity to be considered when fabricating lab-based platforms. Additionally, alternative cancer treatments have arisen with the aim of enhancing drug delivery and reducing the side effects generated by traditional, more aggressive treatments such as chemotherapy. One such treatment consists of the systemic injection of microbubbles together with drug agents that, when exposed to ultrasound, locally enhance drug uptake through sonoporation. This approach requires full understanding of the dynamics of microbubble oscillation and its interaction and effects on the vessel wall, which are highly reliant on microvascular morphology. Reductionist methods for designing phantoms, through simplification of vessel geometry and connectivity, lose in the accuracy of the physics of fluid flow what they gain in manufacturing feasibility. Phantoms in which one can maintain complexity at a small scale and control geometries is vital to determine, both quantitatively and qualitatively, how microvascular features influence blood flow and, ultimately, the transport of compounds into the surrounding tissues.

The ability to produce low-cost, *in-vitro* systems with properties that mimic real tissue offers significant benefits for biomedical research, and recent advances made in light responsive hydrogels have assumed huge importance^{7,8}, providing the tools to develop new platforms for controlled microvascular investigations⁷⁻¹⁰. The fabrication of 3D microvascular topologies is not currently possible within tissue-like materials through any other means. Hydrogels have established applications in cell culture¹⁰⁻¹⁶ and therefore offer the potential for incorporating cells within 3D-printed systems¹⁰. While such platforms have convincingly demonstrated proof of principle and the ability to replicate complex features, those that have employed polyethylene glycol (PEG) hydrogels have been limited by the resulting printing resolution, with enclosed features that have dimensions of hundreds of microns and are therefore not capable of representing the microvasculature^{10,17-19}. Other hydrogel compositions have reported the ability to 3D-print complex branched networks with microchannel diameters below 100 μm , but are not cell-compatible, lack three-dimensional complexity, or do not present mechanical and acoustic properties suitable for exploitation in biomedical research²⁰⁻²². While many factors must be considered when selecting hydrogels for biomedical research, high molecular weight PEG-based hydrogels are commonly used for their accurate replication of tissue elastic moduli^{23,24,25-27}. Unfortunately, these polymers are extremely expensive. Meanwhile, lower molecular weight PEG hydrogels, though more affordable, have less favourable characteristics, with comparatively high compressive strength, but lower tensile strength making them prone to fracture²⁸. Other formulations have further limitations, such as: (i) the type of pattern that can be 3D-printed, and (ii) a reliance on complex and expensive equipment and materials to enhance the resolution in the vertical axis (*z* axis)²⁹⁻³¹. The result is that low molecular weight hydrogels cannot easily be applied to replicate tissue mechanical properties.

In this work we approach this problem using bisphenol-A ethoxylate dimethacrylate (BEMA). The mechanical properties of this compound depend both on its molecular weight and its ethoxylate (EO) per phenol ratio³². While it has been demonstrated that acrylate monomers cause significant cytotoxicity³³⁻³⁵, it has also been proven that methacrylates present significantly lower cytotoxicity³⁵. This factor, together with previous work demonstrating the suitability of BEMA to 3D-printing^{17,36}, has led us to use this polymer to develop a novel hydrogel. We demonstrate that BEMA hydrogels provide a non-cytotoxic platform with mechanical properties well suited for replicating *in vivo* scenarios. This

feature, combined with the ability to manufacture them in a cost-efficient manner, indicates that these materials offer significant prospects for deployment in biomedical research.

Materials and Methods

Preparation of BEMA hydrogel resins and 3D-printing optical calibration

Bisphenol-A ethoxylate dimethacrylate (BEMA, 1.7 kDa, 15 EO/phenol, Sigma Aldrich) hydrogels were prepared by dissolving the polymer in de-ionized water (20 % w/w). 39 mM of lithium phenyl-2,4,6-trimethylbenzoylphosphinate (LAP, Sigma Aldrich) was added to the polymer solution under constant stirring. After full dissolution of LAP, 8.63 mM of tartrazine was added to the solution. The mixture was stirred for 30 min before transferring to the commercial 3D printer (ASIGA Pico2HD27UV, working principle sketched in Fig. 1A). The ASIGA Pico2HD27UV is a direct light processing 3D printer that projects images onto a light-curable liquid resin after lowering the build platform (Fig. 1A1). Once the projected image meets the resin (Fig. 1A2) it solidifies and forms a single layer. After this, a slider (Fig. 1A3) wipes excess resin from the build. After a layer is formed, the build platform is lifted and separated from the bottom of the vat and approaches again to form the next layer by repeating the process until the final part is fully built.

The resin was placed in the 3D printer vat and calibrated using the Beer-Lambert law (Supplemental Material, SM). The thicknesses of the 3D-printed membranes used to calibrate the material were measured using X-ray microcomputed tomography (details in SM).

Measurement of mechanical properties of 3D-printed hydrogels

The elastic modulus (E) of the hydrogel was determined by rheology and nanoindentation.

Rheological measurements were carried out using a stress-controlled rheometer (MCR, Anton Paar) with a parallel plate geometry (upper plate diameter, 15 mm) at room temperature. Strain sweeps in the range of 0.01% to 1% and angular frequency of 10 rad⁻¹ were performed to determine the elastic shear modulus of the material.

Nanoindentation measurements were performed using a nanoindentation device (Chiaro, Optics11, Amsterdam, NL) mounted on top of an inverted phase contrast microscope (Evos XL Core, Thermofisher, Paisley, UK). Measurements were performed in 15x15 arrays at a speed of 2 $\mu\text{m/s}$ over a vertical range of 10 μm . The selected cantilever had a stiffness of 0.032 N/m and held a spherical tip of 8 μm in radius. The data acquired was analysed using custom software programmed in Python 3.0 (Python Software Foundation). The indentation depth was calculated from the penetration-load

curves obtained from nanoindentation assays and the mechanical properties were obtained by fitting the experimental data using the Hertz model.

Acoustic characterisation of 3D-printed BEMA hydrogels

Acoustic measurements were performed to determine the speed of sound. A block of hydrogel was 3D-printed (30mm x 30 mm x 5 mm) as a test object. An ultrasonic transducer (Olympus, A304S-SU) with a centre frequency of 2.25 MHz was used. In anticipation of the speed of sound being approximately that of water, 2.25 MHz was chosen to ensure that the material to test was several wavelengths thick. The transducer was driven by a pulser (WaveMaker, Macro Design Ltd.) in pulse-echo mode, and the output connected to an oscilloscope (Tektronix, DPO4054B). To test the material, the hydrogel sample, stored in water and thus in its swollen state, was briefly removed from storage and placed directly on the transducer face. There was sufficient moisture remaining on the material to provide a full water coupling between transducer and device. Settings for energy, damping, and attenuation on the pulser were adjusted to ensure the resultant signal was not saturated but presented a good signal-to-noise ratio. The presence of the material provides a simple reverberant system with an ultrasonic pulse bouncing between the outer face of the material (hydrogel-air boundary), and the inner face of the material (hydrogel-transducer boundary). Time traces on the oscilloscope were used to calculate the time between successive echoes. The onset of the pulse was used to establish timings for the first and second echo. The speed of sound was calculated from the time difference between first and second echo and the distance the pulse had travelled (twice the material thickness). Time differences were measured by cross-correlation³⁸ of the transmitted and received signals.

Results

Resin preparation and direct light processing

BEMA photo-responsive hydrogels (20 % w/w) were assessed for rapid prototyping of high-resolution microchannels.

Initial 3D-printing tests using this formulation resulted in a 300 μm void feature size and 50 μm membrane thickness, as shown in Fig. 1C (CAD file shown in Fig. 1B for comparison). Optical calibration of the photo-responsive resin was performed by removing the build block and exposing the liquid resin to the 385 nm wavelength light at a set of energies ranging from 498 mJ/cm^2 to 998 mJ/cm^2 . Each of the energies within this set generated a different photo-cured layer thickness, from

103 μm to 144 μm , as shown in Fig. 1D. This process is well-defined by the Beer-Lambert law (see SM) and provides information about the characteristic penetration depth of the resin, D_p (\pm s.e., $N = 308$), which was measured to be of 57.59 (± 1.50) μm . This characteristic depth defines the thickness of the material required to decrease the light intensity to $1/e$ of the intensity at the surface. Plotting C_d versus energy (Fig. 1D) on a semi-logarithmic scale yields a straight line with D_p as the slope of the curve. The critical energy (E_c , which corresponds to the minimum amount of energy required to cure the resin) can be obtained from Fig. 1D by determining the intersection of the curve with the abscissa¹⁷. E_c (\pm s.e., $N = 308$) was established to be of 83.62 (± 0.25) mJ/cm^2 . This data can be used to determine the energy required to cure layers of different thicknesses, allowing fine-tuning of the 3D-printing process to obtain higher printing resolutions. With D_p and E_c determined, the influence of the number of 3D-printed layers below a void feature on the final channel dimensions can be investigated. Samples were printed to contain 5 square channels (500 x 500 μm cross section) placed at heights from 100 μm to 900 μm in steps of 200 μm (Fig. 1E), at layer thickness (l_z) of 10 μm . Using these settings, the differential percentage channel occlusion was found to increase by approximately 1% every 20 layers (Fig. 1F). Channel occlusion arises from continuous exposure of the layers printed below the microchannel and depends on both the absorption properties of the resin and the number of layers printed. The accumulated cure depth will be proportional to $\sum_{n=0}^N E_0 e^{-nl_z/D_p}$, where E_0 is the energy received at the bottom of the vat, and n the number of layers printed below the channel. A good approximation of the accumulated cure depth can be obtained by applying the partial sum formula, leading to $\sum_{n=0}^N E_0 e^{-nl_z/D_p} = (e^{-Nl_z/D_p} - A)/B$, where $A = e^{-l_z/D_p}$, and $B = 1 - A$. This information was used to develop CAD files that allow detailed reproduction of 3D microchannel structures (Fig. 2). The results of this process are presented in Fig. 2A and Fig. 2B. In the former, the model predicted 246 μm channels while the 3D-printed feature measured (\pm s.e., $N = 5$) 229.6 (± 4.9) μm . In Fig. 2B, the model predicted straight channel diameters of 175 μm while the 3D-printed feature measured 154.4 (± 6.8) μm (microscope images of characteristic regions, under bright field, x10 magnification, are shown in Figs. 2C and 2D). Around this channel, we 3D-printed a helical channel with varying diameters (CAD file shown in Figs. 2E and 2F) with measured diameters from 371.3 (± 8.8) μm to 263.5 (± 30.8) μm , depending on the number of layers printed below (Figs. 2G-J, bright field images, x10 magnification). These correlated to predicted diameters of 382.5 μm and 280 μm , respectively.

Acoustic and mechanical characterisation of the hydrogel

BEMA hydrogels were fully characterized through assessment of their swelling volumetric ratio (Q_v)²⁵, speed of sound, and Young's modulus. Fig. 3A shows the swelling analysis where 3 rectangular samples were isolated and measured every 15 minutes for 4 hours, left overnight under standard atmospheric conditions, and measured the following day at 30 min intervals over 5 hours to obtain a Q_v (\pm s.e., $N = 3$) of 4.48 (\pm 0.22). Q_v is directly related to the degree of porosity (χ) of the hydrogel³⁷, which was estimated using Flory's theory to be within the range of 0.7 to 2 nm. This is important because it provides an indication of how the hydrogel might perform as a medium for nutrient transport within biomedical systems. Flory's theory requires knowledge of several molecular characteristics of the polymer, which were obtained from the literature (see SM).

An ideal material for reconstructing phantoms for biomedical research should have a range of speeds of sound similar to the ranges found in soft tissue (e.g. 1440 – 1600 m/s^{39,40}). The speed of sound of the hydrogel, determined using cross-correlation, was calculated to be of 1394.6 (\pm 0.2) m/s (with $N = 3$). Point measurements of the pulse-echo response shown in Fig. 3B indicate that the speed of sound is between 1387.4 m/s and 1566.5 m/s, and comparable to the speed of sound of tissue. The density of the hydrogel was measured to be (\pm s.e., $N = 3$) 1110.8 (\pm 20.2) kg/m³. Young's modulus (E) was determined from stress-controlled rheology ($N = 62$) and nanoindentation ($N = 468$), providing values of E (\pm s.e.) of 51.78 (\pm 0.75) kPa, and 55.65 (\pm 1.87) kPa, respectively (SM, Fig. 1).

Cell attachment and growth on BEMA hydrogels

To confirm that the hydrogels did not present a source of cytotoxicity, cultured smooth muscle cells (SMCs) were seeded into wells containing BEMA hydrogel droplets (as described in SM). As expected from the literature⁴¹ the SMCs did not adhere to the BEMA surface. However, they grew to confluence on the surrounding tissue culture plastic (TCP) substrate, indicating no cytotoxic effects from the BEMA hydrogel (Fig. 4). Modified BEMA hydrogel substrates were also tested to assess whether they could support cell growth. Coating the surface of the cured BEMA hydrogel or bulk doping the hydrogel formulation with collagen (type I, acid solubilised) did not enable long-term attachment and proliferation (Figs. 4B-E), though short-term attachment was enhanced (Fig. 4B). Doping of the BEMA hydrogel with poly(vinyl alcohol) (PVA), which has previously been used in hydrogel formulations to support cell growth⁴², was more promising, with patches of SMCs remaining viable after 11 days in culture. However, cell morphologies indicated weak attachment and

proliferation was low in comparison to TCP controls. Nonetheless, these results confirm the cytocompatibility of BEMA hydrogels and suggest that other hydrogel doping strategies^{43,44} could be exploited to enable strong cell attachment and growth, a study that we are currently undertaking to better understand how to produce fully 3D-printed, cell-laden platforms.

Discussion

We report the characterization and demonstration of BEMA hydrogels, which we propose as an improved medium for 3D-printing over the higher molecular weight PEG-based hydrogels, commonly used for applications in biomedical research. The use of BEMA as a base polymer results in a cost-effective material that is well suited to 3D-printing of tissue-mimicking, non-cytotoxic materials. We demonstrate its application to generate three dimensional microchannels with functional characteristic channel diameters down to 150 μm .

Small diameter channels were obtained after calibration of the photo-responsive resin; characteristic parameters of the resin revealed that, when developing microchannel systems, the differential percentage of channel occlusion increases by 1% every 20 print layers. This is a feature that needs to be characterised at each l_z . Although there is a part of microchannel occlusion that results from cumulative cure depth, and thus exposure to residual ultraviolet (UV) light, there are other factors that may influence the final degree of channel occlusion, including l_z , D_p , E_c , and the resin's viscosity. The high water content of the hydrogel formulation is hypothesized to play an important role in the kinetics of UV-based light-based 3D-printing processes. Water is a well-known UV absorber and as such the hydrogel composition highly influences the kinetics of the reaction taking place and therefore requires fine tuning. Further investigation of how these parameters introduce variability in the print-curing process, and how this can be described mathematically, will allow further refinement of the 3D-printing resolutions and feature size predictability and repeatability.

Swelling measurements indicate that the BEMA hydrogels take up 4.14 g of solvent per gram of polymer, leading to Q_v values that can be used to determine their mesh size (χ). The χ values obtained were similar to those of similar PEG-based hydrogel composition^{45,46}. Mechanical characterization of the hydrogels revealed an elastic modulus of 55 kPa, which was confirmed by rheology and indentation measurements, and indicates a good match to the mechanical properties of soft tissue⁴⁷. The mechanical properties of the 3D-printed hydrogels can be modified by selectively changing the amount and content of the resin used, as well as using polymers of different molecular

weights (MW), where higher MW lead to lower E values and *vice versa*. This process allows for fine tuning of the mechanical properties of the 3D-printable material to match tissue stiffnesses of interest, potentially leading to multi-material tissue-mimicking 3D-printing.

These results provide a strong basis to suggest that this new hydrogel approach provides a promising alternative to PEG-based methodologies. As expected, unmodified BEMA hydrogels did not support cell attachment and growth. However, they are non-cytotoxic and have shown potential to support cell growth with suitable modifications, as suggested by results obtained with PVA-doped BEMA hydrogels.

Methods that have been used to modify PEGDA hydrogels to support cell attachment^{10,44,47} could be similarly exploited to enable adhesion to BEMA hydrogels. Example strategies for future investigation include doping of BEMA hydrogels with GelMA^{10,48} or acrylic acid^{44,47} or covalent coupling of peptide motifs via the terminal methacrylate groups^{49,50}, ultimately enabling the creation of high resolution, cell-laden, physiologically-relevant microvascular phantoms. These processes form the main body of our current investigation in order to develop a fully 3D-printed, cell-laden platform.

Conclusions

We show that BEMA hydrogels can be used to 3D-print high-resolution microchannels and provide a non-cytotoxic environment that supports cell adhesion. The acoustic and mechanical properties of the BEMA hydrogels are comparable to soft tissue^{34,38}. These values indicate that the high water content of BEMA hydrogels lead to new tissue-mimicking photo-responsive resins that can be rapidly and cheaply produced for complex three-dimensional, high-resolution microchannel 3D-printing. While the mechanical properties of the hydrogel reproduce tissue properties to establish a reliable platform for biomedically relevant experimentation, acoustic properties open opportunities to use this platform for controlled ultrasound-based investigation within a range of dimensions that replicate microvascular features.

Acknowledgments

The authors would like to thank Dr. Andrew Reid for technical support and Mr. Euan Foster for assistance in measuring the acoustic properties of the photosensitive hydrogels, Dr. Manlio Tassieri and Dr. Massimo Vassalli for equipment (rheometer and nanoindenter), and Mr. Giuseppe Ciccone for his assistance in Python.

Authorship confirmation statement

Authors' disclosure statement

No competing financial interests exist.

Funding Statement

The authors would like to acknowledge funding from the Biotechnology and Biological Sciences Research Council (BBSRC, BB/T012102/1).

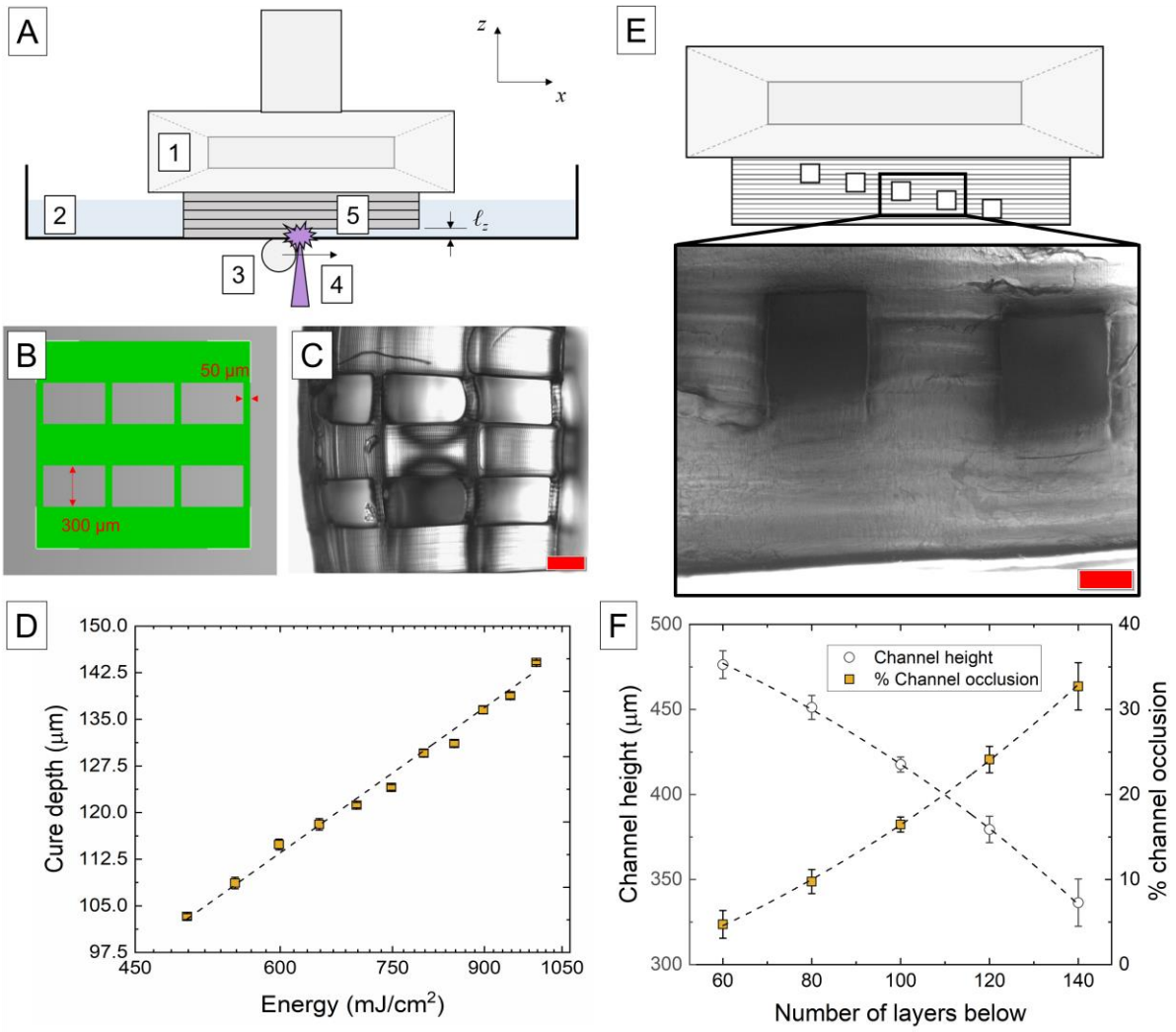
References

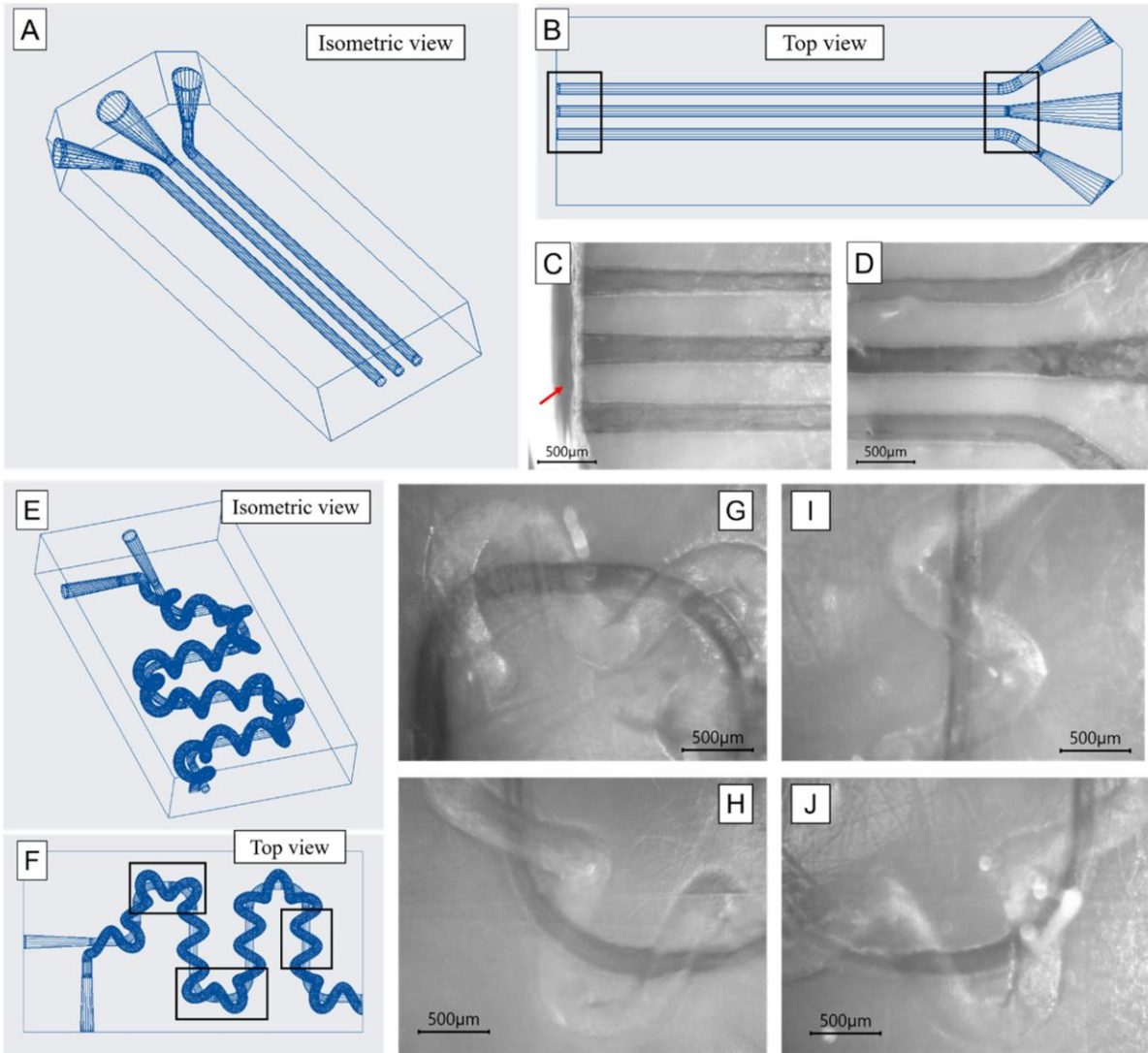
1. Schonfeld F, Hardt S. Simulation of helical flows in microchannels. *AIChE J* 2004;50:771-778.
2. Sefidgar M, Soltani M, Raahemifar K, et al. Numerical modeling of drug delivery in a dynamic solid tumor microvasculature. *Microvas. Res* 2015;99:43-56.
3. Di Gregorio S, Fedele M, Pontone G, et al. A computational model applied to myocardial perfusion in the human heart: From large coronaries to microvasculature. *J Comp Phys* 2021;424:109836.
4. Rossinelli D, Tang YH, Lykov K, et al. The in-silico lab-on-a-chip:petascale and high-throughput simulations of microfluidics at cell resolution. *International Conference for High Performance Computing, Networking, Storage and Analysis*. 2015. Austin. 1-12.
5. Penta R, Ambrosi D. The role of the microvascular tortuosity in tumor transport phenomena. *J Theor Biol* 2015;364:80-97.
6. Dewhirst MW, Secomb TW. Transport of drugs from blood vessels to tumour tissue. *Net Rev Cancer* 2017;12:738-750.
7. Green BJ, Worthington KS, Thompson JR, et al. Effect of molecular weight and functionality on acrylated poly (caprolactone) for stereolithography and biomedical applications. *Biomacromolecules* 2018;19:3682-3692.
8. Schmidleithner C, Malferrari S, Palgrave R, et al. Application of high resolution DLP stereolithography for fabrication of tricalcium phosphate scaffolds for bone regeneration. *Biomed Matter* 2019;14:045018.
9. Domingo-Roca R, Saltin B, Winfmill JFC, et al. Rapid prototyped microvessel flow phantom for controlled investigation of ultrasound-mediated targeted drug delivery. *IEEE International Ultrasonics Symposium*. 2019. Glasgow. 2390-2393.
10. Grigoryan B, Paulsen SJ, Corbett DC, et al. Multivascular networks and functional intravascular topologies within biocompatible hydrogels. *Science* 2019;364:458-464.
11. Pereira RF, Bartolo PJ. Photopolymerizable hydrogels in regenerative medicine and drug delivery. *Future Sci* 2014;6-28.
12. Raman R, Bashir R. Stereolithographic 3D bioprinting for biomedical applications. In: *Essentials of 3D Biofabrication and Translation*. Academic Press, 2015, pp. 89-121.

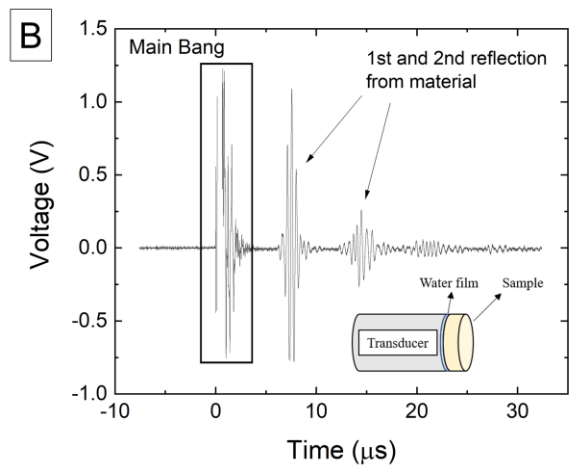
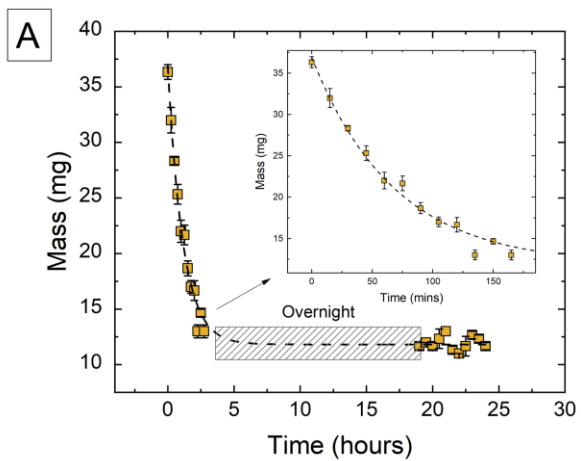
13. Lee KY, Mooney J. Hydrogels for tissue engineering. *Chem Rev* 2001;101:1869-1880.
14. Hoare TR, Kohane DS. Hydrogels in drug delivery: Progress and challenges. *Polymer* 2008;49:1993-2007.
15. Nicodemus GD, Bryant SJ. Cell encapsulation in biodegradable hydrogels for tissue engineering applications. *Tissue Eng Part B Rev* 2008;14:149-164.
16. Kadilak AL, Rehaag JC, Harrington CA, et al. A 3D-printed microbial cell culture platform with in situ PEGDA hydrogel barriers for differential substrate delivery. *Biomicrofluidics* 2017;11:054109.
17. Gong H, Beauchamp M, Perry S, et al. Optical approach to resin formulation for 3D printed microfluidics. *RSC Adv* 2015;5: 106621-106632.
18. Benjamin AD, Abbasi R, Owens M, et al. Light-based 3D printing of hydrogels with high-resolution channels. *Biomed Phys Eng Express* 2019;5:025035.
19. Domingo-Roca R. 3D-Printing technology applied to the development of bio-inspired functional acoustic systems. Doctoral Thesis, University of Strathclyde, 2018.
20. Branderberg N, Lutolf MP. In situ patterning of microfluidic networks in 3D cell-laden hydrogels. *Adv. Mater.* 2016;28:7450-7456.
21. Xie R, Zheng W, Guan L, et al. Engineering of hydrogel materials with perfusable microchannels for building vascularized tissues. *Small* 2020;16:1902838.
22. Wu W, DeConinck A, Lewis JA. Omnidirectional printing of 3D microvascular networks. *Adv. Mater.* 2011;23:H178-H183.
23. Lutolf MP, Lauer-Fields JL, Schmoekel HG, et al. Synthetic matrix metalloproteinase-sensitive hydrogels for the conduction of tissue regeneration: Engineering cell-invasion characteristics. *Proc Natl Acad Sci USA* 2003;100:5413-5418.
24. Phelps EA, Enemchukwu NO, Fiore VF, et al. Maleimide cross-linked bioactive peg hydrogel exhibits improved reaction kinetics and cross-linking for cell encapsulation and in situ delivery. *Adv Mater* 2012;24:64-70.
25. Cailari SR, Burdick JA. A practical guide to hydrogels for cell culture. *Nat Methods* 2016;14:405-414.
26. Kloxin AM, Kasko AM, Salinas CN, et al. Photodegradable hydrogels for dynamic tuning of physical and chemical properties. *Science* 2009;324:59-63.
27. Moon JJ, Saik JE, Poche RA, et al. Biomimetic hydrogel with pro-angiogenic properties. *Biomaterials* 2010;31:3840-3847.
28. Ye D, Chang C, Zhang L. High-strength and tough cellulose hydrogels chemically dual cross-linked by using low-and high-molecular-weight cross-linkers. *Biomacromolecules* 2019;20:1989-1995.
29. Hahn MS, Miller JS, West JL. Three-dimensional biochemical and biomechanical patterning of hydrogels for guiding cell behavior. *Adv Mater* 2006;18:2679-2684.

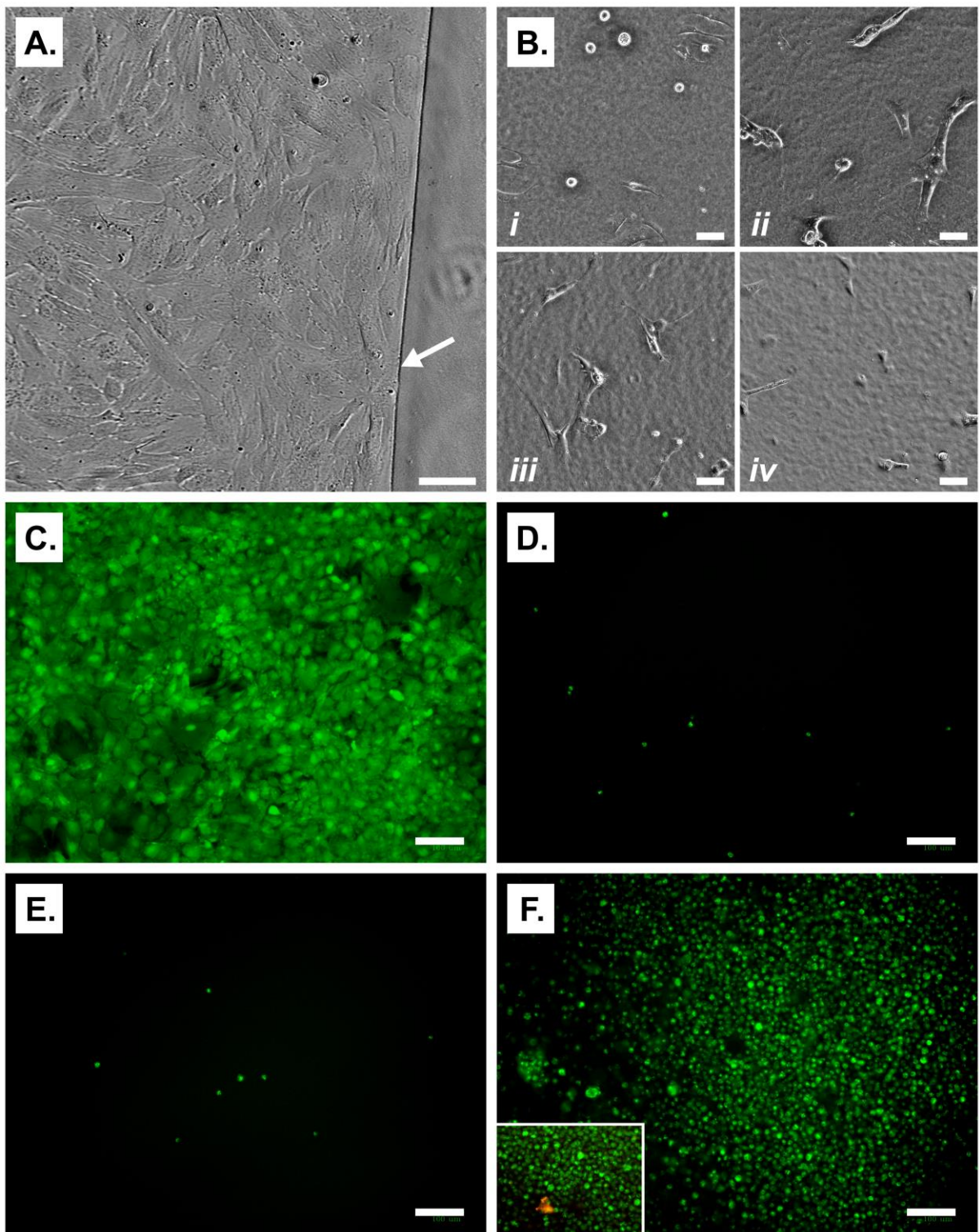
30. DeForest CA, Anseth KS. Compatible click-based hydrogels with dynamically tunable properties through orthogonal photoconjugation and photocleavage reactions. *Nat Chem* 2011;3:925-931.
31. Heintz KA, Bregenzer ME, Mantle JL, et al. Fabrication of 3D biomimetic microfluidic networks in hydrogels. *Adv Healthc Mater* 2016;5:2153-2160.
32. Richards JJ, Danquah MK, Kalakkunnath S, et al. Relation between structure and gas transport properties of polyethylene oxide networks based on crosslinked bisphenol A ethoxylate diacrylate. *Chem Eng Sci* 2009;64:4707-4718.
33. Heller C, Schwentenwein M, Russmueller G, et al. Vinyl esters: low cytotoxicity monomers for the fabrication of biocompatible 3D scaffolds by lithography based additive manufacturing. *J Polym Sci A Polym Chem* 2009;47:6941-6954.
34. Qin XH, Ovsianikov A, Stampfl J, et al. Additive manufacturing of photosensitive hydrogels for tissue engineering applications. *Bionanomaterials* 2014;15:49-70.
35. Wang X, Qin XH, Hu C, et al. 3D printed enzymatically biodegradable soft helical microswimmers. *Adv Funct Mater* 2018;28:1804107.
36. Domingo-Roca R, Tiller B, Jackson JC, et al. Bio-inspired 3D-printed piezoelectric device for acoustic frequency selection. *Sensor Actuat A-Phys* 2018;271:1-8.
37. Chan V, Zorlutuna P, Jeong JH, et al. Three-dimensional photopatterning of hydrogels using stereolithography for long-term cell encapsulation. *Lab Chip* 2010;10:2062-2070.
38. Jakovljevic M, Hsieh S, Ali R, et al. Local speed of sound estimation in tissue using pulse-echo ultrasound: Model-based approach. *J Acous Soc Am* 2018;144:254-266.
39. Madsen EL, Zagzebski JA, Banjavie RA, et al. Tissue mimicking materials for ultrasound phantoms. *Med Phys* 1978;5:391-394.
40. ITIS Foundation. Tissue properties: speed of sound. <https://itis.swiss/virtual-population/tissue-properties/database/acoustic-properties/speed-of-sound/>
41. Moore EM, West JL. Bioactive poly(ethylene glycol) acrylate hydrogels for regenerative engineering. *Regen. Eng. Transl. Med.* 2019;5:167-179.
42. Kim HD, Lee Y, Kim Y, et al. Biomimetically reinforced polyvinyl alcohol-based hybrid scaffolds for cartilage tissue engineering. *Polymers* 2017;9:655-671.
43. Browe DP, Wood C, Sze MT, et al. Characterization and optimization of actuating poly(ethylene glycol) diacrylate/acrylic acid hydrogels as artificial muscles. *Polymer* 2019;117:331-341.
44. Castano AG, Garcia-Diaz M, Torras N, et al. Dynamic photopolymerization produces complex microstructures on hydrogels in a moldless approach to generate a 3D intestinal tissue model. *Biofabrication* 2019;11:025007.

45. Yang T. Mechanical and swelling properties of hydrogels. Doctoral dissertation. KTH Royal Institute of Technology. 2012.
46. O'Donnell K, Boyd A, Meenan BJ. Controlling fluid diffusion and release through mixed-molecular-weight poly(ethylene) glycol diacrylate (PEGDA) hydrogels. *Mater.* 2019;12:3381.
47. Handorf A, Zhou Y, Halanski MA, et al. Tissue stiffness dictates development, homeostasis, and disease progression. *Organogenesis* 2015;11:1-15.
48. Wang Y, Ma M, Wang J, et al. Development of a photo-crosslinking, biodegradable GelMa/PEGDA hydrogel for guided bone regeneration materials. *Mater.* 2018;11:1245-1257.
49. Zhu J, Tang C, Kottke-Marchant K, et al. Design and synthesis of biomimetic hydrogel scaffolds with controlled organization of cyclic RGD peptides. *Bioconj. Chem.* 2009;20:333-339.
50. Ingavle GC, Gehrke SH, Detamore MS. The bioactivity of agarose-PEGDA interpenetrating network hydrogels with covalently immobilized RGD peptides and physically entrapped aggrecan. *Biomaterials* 2014;35:3558-3570.









3D-Printing of non-cytotoxic high-resolution microchannels in Bisphenol-A tissue-mimicking materials – Figure Captions

Figure 1. (A) Illustration of a direct light processing-based 3D printer and its main components: A1) build block, where the 3D-printed part is attached, A2) photoreactive resin (hydrogel) sitting on the build tray, A3) slider which moves in the x direction and removes resin excess, A4) light projected into the resin, and A5) the 3D-printed layers, of thickness l_z , forming the 3D-printed part. (B) The CAD file used to 3D-print a test structure. (C) Bright field optical microscopy image of the 3D-printed sample (scale bar = 200 μm). (D) Plot showing the single layer cure depth as a function of energy for BEMA hydrogel, with $c_b = 0.4 \text{ mg mL}^{-1}$. The dashed line fits the experimental data (squares \pm s.e.) according to Eq.(1), with $R^2 = 0.9932$, and with N (number of samples) plotted in the secondary y axis. (E) Schematic representation of the 500x500 μm (cross section) channels at different heights such that a different number of layers was printed below each of them. Bright field image of two of the corresponding channels (scale bar = 200 μm). (F) Shows the channel height and percentage of channel occlusion as a function of the number of layers that are 3D-printed below each channel. All channels were modelled to be 500 μm . $N = 4 \pm$ s.e.

Figure 2. (A) and (B) isometric and top view, respectively, of the CAD file used to 3D-print microchannels positioned 350 micron apart. (C) and (D) show optical microscope images of the inlet and outlet (250 μm diameter) of the 3D-printed microchannels, corresponding to the boxes shown in (B). The darker microchannel colour is caused by the presence of a dye used to aid channel visualization and differentiation. The red arrow in (C) indicates fluid emerging from the microchannel. (E) and (F) show the isometric and top view, respectively, of the CAD file used to 3D-print a microchannel (250 μm diameter) surrounded by an air-filled helix (450 μm diameter). (G) to (J) show optical microscope images of the boxes highlighted in (F). It can be observed that all microchannels are fully open, where a dye has been used in only one microchannel to ease visualization and differentiation.

Figure 3. (A) De-swelling kinetics of the 3D-printed BEMA hydrogel through mass variation over time ($N = 3 \pm$ s.e.). The hydrogels were initially measured when fully hydrated (immediately post 3D-printing) at intervals of 15 minutes for 4 hours prior to being left under atmospheric conditions

overnight. The final set of measurements were made every 30 minutes for 5 hours. The data was fitted using an exponential decay function ($R^2 = 0.9748$). (B) The acoustic pulse-echo response in time. A transducer with centre frequency 2.25 MHz in direct contact with the BEMA hydrogel transmits an acoustic pulse into the material (as shown schematically in the bottom-right). The transit time of the acoustic pulse was measured for the first and second echo using the cross-correlation method, leading to a speed of sound, $c = 1391$ m/s.

Figure 4. SMCs cultured in wells with 10% BEMA droplets (A-B, scale bar 50 μm) grew to confluency upon the surrounding TCP regions, abutting against the BEMA droplets (A, arrow indicating the droplet edge) but not growing upon the BEMA surface. When the droplets were coated with collagen (B), SMCs initially adhered to the droplet surface (i-ii, showing 2 h and 2 days post-seeding) but cell adhesion decreased with time and cell growth was not ultimately supported (iii-iv, showing 4 days and 7 days post-seeding). Doped hydrogel experiments (C-F, showing staining on day 11 with calcein-AM, green, scale bar 100 μm), with a TCP control well (C), showed similar results to the droplet tests for undoped BEMA (D, 20% BEMA) and collagen-doped BEMA (E), with no evidence of cell attachment or growth over time. PVA-doped BEMA (F) showed signs of improved cell support, with regions of viable cells remaining upon the surface for the 11 day culture period, although the more rounded morphology of these cells indicated weak attachment and overall cell proliferation was low. PI staining was negligible for undoped and collagen-doped BEMA and only rare instances were seen for the PVA-doped BEMA (inset F, PI shown in red).

3D-Printing of non-cytotoxic high-resolution microchannels in Bisphenol-A tissue-mimicking materials – Supplemental Material

Roger Domingo-Roca^{*a}, Lauren Gilmour^a, Oana Dobre^c, Stylianos Sarrigiannidis^c, Manuel Salmeron-Sanchez^c, Mairi E. Sandison^a, Richard O’Leary^b, Joseph C. Jackson-Camargo^c, Helen E. Mulvana^a

^a Department of Biomedical Engineering, University of Strathclyde, Glasgow.

^b Department of Electronic and Electrical Engineering, University of Strathclyde, Glasgow.

^c James Watt School of Engineering, University of Glasgow, Glasgow.

* Corresponding author: Roger Domingo-Roca, 106, Rottenrow Street, G4 0NW, Glasgow, roger.domingo-roca@strath.ac.uk

Email list: lauren.gilmour@strath.ac.uk, oana.dobre@glasgow.ac.uk, 2022917S@student.gla.ac.uk, manuel.salmeron-sanchez@glsgowa.ac.uk, mairi.sandison@strath.ac.uk, richard.o-learny@strath.ac.uk, joseph.jackson@strath.ac.uk, helen.mulvana@strath.ac.uk

1. Background Theory
2. Supplemental Methods
3. Supplemental Figures
4. References

1. Background Theory

Optical calibration of the hydrogels for direct light processing

Direct light processing (DLP) machines build up parts in a layer-by-layer fashion by exposing each layer to light for a controlled amount of time. This exposure time, combined with the intensity of the light source, determine the energy delivered to the resin. As each layer of resin is exposed, the previously 3D-printed layers still receive a residual dose of light that may lead to over-curing of the 3D-printed sample and therefore result in a loss of resolution. The dose received by each previously printed layer will depend, mainly, on the amount of photoblocker and viscosity of the resin. The exposure profile in the z-direction is given by Eq. (1)¹⁻³:

$$E(z) = E_0 e^{-z/D_p} \quad (1)$$

where E_0 is the energy received at the bottom of the resin tray just as the light enters the resin ($z=0$). D_p is the penetration depth, which is the length scale that characterizes the exponential decay. The cure depth, C_d , beyond which the resin remains liquid is determined by the critical energy, E_c , which can be determined by setting $z = C_d$ in Eq. (1). Solving Eq. (1) for C_d and plotting it against the delivered energy in a linear-log scale provides information about the optical properties of the resin¹⁻³. These can be

related to the energy profile through the Beer-Lambert law, which associates the absorbance of light to the absorptivity coefficient, ϵ , and photoblocker concentration, c_b .

$$C_d = \ln(E_0/E_c)/(\epsilon c_b) \quad (2)$$

Equation (2) provides information about C_d as a function of c_b . From this relationship it follows that, for the same resin, increasing the amount of photoblocker will lead to lower C_d values. Furthermore, as c_b is increased, in general, better resolution will be obtained but higher energies will be required to cure a single layer, impacting production time.

When 3D-printing microchannels, layers are continuously built under the channel; as more layers are built below the channel, additional energy is provided to previously printed layers, referred to as *cumulative energy*. This extra energy results in an accumulated cure depth, $C_{d,c}$, that leads to microchannel occlusion.

$$E_{0,c} = \sum_{i=0}^n E_0 10^{-\epsilon c_b i l z} \quad (3)$$

$$C_{d,c} = D_p \ln(E_{0,c}/E_c) \quad (4)$$

Equations (3) and (4) provide enough information about the characteristic parameters of the resin used such that compensation factors can be introduced when designing a CAD file and improve the resolution of the final 3D-printed sample.

Swelling measurements and mesh size calculation of 3D-printed BEMA hydrogels

Swelling is defined as the amount of water taken up into the hydrogel and provides an indication of the hydrophilicity of the polymer network, and well as an indication of the relative crosslink density, with stiffer networks exhibiting lower swelling⁷. The mass-swell ratio (Q_m) is defined as the ratio of wet to dry weight (M_w and M_d , respectively), while the volumetric swelling ratio (Q_v) can be determined from Q_m and both the hydrogel and solvent densities (Eq. (5)).

$$Q_v = 1 + \frac{\rho_{hg}}{\rho_s} \left(\frac{M_w}{M_d} - 1 \right) \quad (5)$$

Q_v is directly related to hydrogel molecular porosity, χ . Smaller mesh sizes relate to lower swelling ratios and higher elastic modulus, and vice versa. The mesh size of step-growth hydrogels can be theoretically determined as a function of several molecular characteristics of the hydrogel^{7,8}.

$$\chi = v_{2,s}^{-1/3} \frac{2M_c C_n}{M_r} l \quad (6)$$

where $v_{2,s}$ is the polymer volume fraction in the swollen state (which can be determined from Eq.(7)), M_c is the molecular weight between crosslinks, C_n is the Flory characteristic length, l is the length of the bond along the polymer backbone, and M_r is the molecular weight of the monomer. As such, $v_{2,s}$ is calculated as.

$$v_{2,s} = \frac{1}{Q \frac{\rho_p}{\rho_{H_2O}} + 1} \quad (7)$$

where Q is the swollen-to-dry ratio. Values of M_c , C_n , l , and M_r were obtained from the literature⁹⁻¹¹.

Table I shows the values used:

Table I: Parameters used to calculate the mesh size of the 3D-printed hydrogel, obtained from the literature.

Parameter ⁹⁻¹¹	Value
M_c (molecular weight between crosslinks)	220 (g/mol)
C_n (Flory characteristic length)	2.2
l (length of the bond)	1.56 Å
M_r (monomer molecular weight)	376.4 (g/mol)

2. Supplemental Methods

X-ray micro computed tomography

X-ray micro computed tomography, μ CT, (Bruker, Skyscanner, 1172) was used to measure membrane thickness. Even though μ CT is a well-established method for imaging mineralized animal tissues⁴, its widespread application in comparative morphology is limited to low intrinsic x-ray contrast of non-mineralized tissues. Iodine has been shown to impart differential x-ray contrast^{5,6}. The calibration membranes were thawed and stained with 1% weight/volume (w/v) Iodine in absolute ethanol (Sigma Aldrich) overnight⁶ and mounted before being scanned in the μ CT at 70 kV, 100 μ A, and pixel size resolution of 2.5 μ m. Flat-field correction was taken prior to scanning to correct pixel sensitivity. Rotational scanning was performed around the vertical axis in rotation steps of 0.4°, and a frame averaging of 2 was applied.

Cell culture methods

Cell culture was initially performed on hydrogel droplets deposited into the centre of a well in a chambered coverslip culture dish (ibiTreat μ -Slide 8 Well, Ibidi, Germany). A wide border of uncoated tissue culture plastic (TCP) remained around each droplet. Samples were UV sterilized (DaRo Steristrom Ultraviolet Disinfection Cabinet) and then incubated in serum-free media (SFM) for 1 hour. Half of the samples were then collagen coated by incubating for 1 h in 50 μ g/mL Type I acid-solubilized collagen (Collagen Solutions, UK) in 17.5 mM acetic acid. All gels were then re-washed with SFM. The gels were seeded with cultured rat aortic smooth muscle cells (SMCs) that had been obtained from freshly isolated tissue by enzymatic digestion and trituration, as previously described³⁷. SMCs were cultured in 1:1 Waymouth's:Ham's F-12 media containing 10% fetal bovine serum with 1% penicillin-streptomycin and 1% L-glutamine at 37°C in 5% CO₂ and 80% humidity. Cells were imaged using phase contrast microscopy on an inverted Nikon Ti-U microscope equipped with a x20 ELWD objective, a pE-100 LED white light source (CoolLED) and an ORCA-Flash4.0LT sCMOS camera (Hamamatsu, Japan) for image capture.

Cell culture experiments were also performed with doped BEMA hydrogels, doping with both collagen (final concentration 2mg/ml collagen, 13.3% BEMA) and poly(vinyl alcohol) (PVA) (final concentration 2.5% PVA, 10% BEMA). The gels were deposited into a 24-well plate such that a thin film covered the

entire base of the well. After curing, the gels were UV sterilised and washed with cell culture media. Cell growth was monitored over a period of 11 days with end-point live-dead staining carried out using propidium iodide (PI, 20 $\mu\text{g}/\text{mL}$) and Calcein-AM (5 μM). Fluorescence imaging was performed using a ZOE Fluorescent Cell Imager with a x10 objective.

3. Supplemental Figures

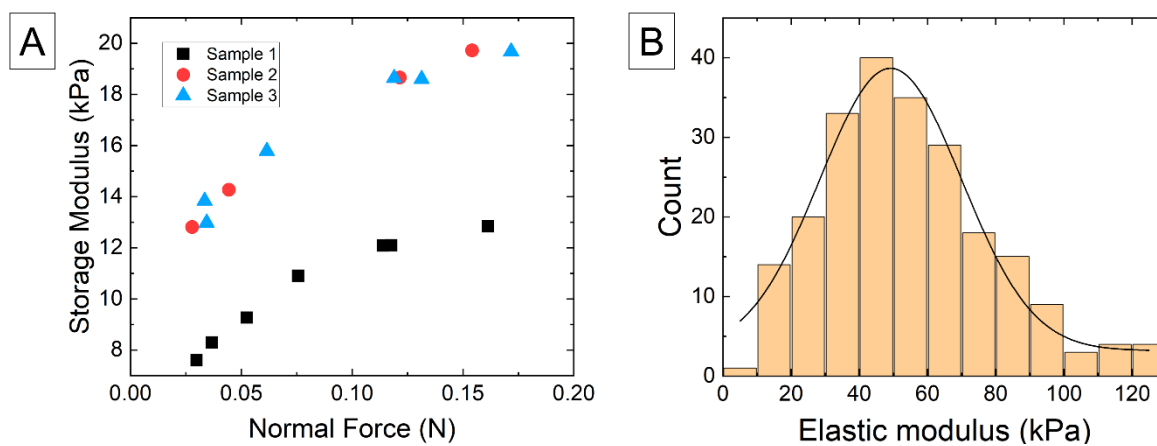


Fig. 1 (A) Storage modulus (in kPa) of three bisphenol-A ethoxylate dimethacrylate hydrogel samples plotted as a function of the testing normal force. (B) Histogram of the measured elastic modulus (E) in nanoindentation experiments, with the corresponding Gaussian fitting function (solid black line).

4. References

1. Grigoryan B, Paulsen SJ, Corbett DC, et al. Multivascular networks and functional intravascular topologies within biocompatible hydrogels. *Science* 2019;364:458-464.
2. Gong H, Beauchamp M, Perry S, et al. Optical approach to resin formulation for 3D printed microfluidics. *RSC Adv* 2015;5: 106621-106632.
3. Benjamin AD, Abbasi R, Owens M, et al. Light-based 3D printing of hydrogels with high-resolution channels. *Biomed Phys Eng Express* 2019;5:025035.
4. Neues F, Epples M. X-ray microcomputer tomography for the study of biomineralized endo- and exoskeletons of animals. *Chem Rev* 2008;108:4734-4741.
5. Domingo-Roca R, Saltin B, Winfill JFC, Jackson J, Mulvana H. Rapid prototyped microvessel flow phantom for controlled investigation of ultrasound-mediated targeted drug delivery. *IEEE International Ultrasonics Symposium*. 2019. Glasgow. 2390-2393.
6. Metscher BD. MicroCT for comparative morphology: simple staining methods allow high-contrast 3D imaging of diverse non-mineralized animal tissues. *BMC Physiol* 2009;9:1-14.
7. Cailari SR, Burdick JA. A practical guide to hydrogels for cell culture. *Nat Methods* 2016;14:405-414.
8. Chan V, Zorlutuna P, Jeong JH, et al. Three-dimensional photopatterning of hydrogels using stereolithography for long-term cell encapsulation. *Lab Chip* 2010;10:2062-2070.
9. Polymer Properties Database. Characteristic ratio of some polymers. 2015-2021.
<http://polymerdatabase.com/polymer%20physics/C%20Table2%20.html>
10. Polymer Properties Database. Two-phase theory. 2015-2021.
<https://polymerdatabase.com/polymer%20physics/2PT.html>
11. Ito A, Semba T, Taki K, et al. Effect of the molecular weight between crosslinks of thermally cured epoxy resins on the CO₂-bubble nucleation in a batch physical foaming process. *J Appl Polym Sci* 2014;12:131-139.